Switchable planar chirality and spin texture in highly ordered ferroelectric hybrid perovskite domains

Chuanzhao Li[1,6], Mykola Telychko[2,6], Yue Zheng[3,6], Shurong Yuan[1], Zhenyue Wu[1], Walter P. D. Wong[4], Yixin Li [1], Yuanyuan Jin[1], Weng Fu Io[1], Xinyun Wang[4], Junhao Lin [5], Jianhua Hao [1], Cheng Han [3] ✉ & Kai Leng [1] ✉

Chiral organic-inorganic hybrid perovskites offer a promising platform for developing non-linear chiro-optical applications and chiral-induced spin selectivity. Here, we show that achiral hybrid perovskites that have highly ordered ferroelectric domains with orthogonal polarization exhibit planar chirality, as manifested by second harmonic generation with strong circular dichroism. Interestingly, the handedness of the second harmonic generation circular dichroism response can be alternatingly switched between orthogonally polarized domains and domain walls. To correlate the origin of planar chirality in these domains, atom-resolved atomic force microscopy is used to reveal distinct arrangements of atomic rows in these ferroelectric crystals that indicate planar symmetry breaking. Remarkably, a large SHG anisotropy factor of 0.41 is measured at the domain wall. Additionally, spatially resolved two-photon photoluminescence excitation measurement provide evidence of larger Rashba spin-splitting in these chiral ferroelectric domains compared to domain-free areas. Our discoveries of domain-dependent planar chirality and spin texture hold great promise for advancement of domain-specific chiro-optical applications.

Chirality refers to the geometric property of a structure that cannot be superimposed on its mirror image, akin to how left and right hands are differ. Molecular chirality arises from the asymmetry of its atomic environment, while planar chirality can result from structural elements that are not inherently chiral but become so through their ordered arrangements that break mirror symmetry. This concept is best exemplified by artificially fabricated planar chiral array, which have been reported to exhibit handedness-sensitive rotations and ellipti-zation of the polarization state[1]. Domain walls (DWs) and domains are prominent microstructural features of ferroelectric materials and possess electronic and symmetry properties that differ from those of bulk crystals[2–5]. Previous research on ferroelectric domains has mainly focused on the dynamics of domain transition and their ferroelastic coupling with DWs[6,7]. However, there remains a lack of understanding regarding the chiro-optical properties of ferroelectric domains and DWs, which can be distinct from achiral bulk crystal owing to local symmetry breaking. There are two levels of chirality that can be explored within ferroelectric domains. Of particular interest is the

[1]Department of Applied Physics, The Hong Kong Polytechnic University, Hung Hom, Kowloon, Hong Kong, China. [2]Center for Nanophase Materials Sciences, Oak Ridge National Laboratory, Oak Ridge, Tennessee 37831, USA. [3]State Key Laboratory of Radio Frequency Heterogeneous Integration, and International Collaborative Laboratory of 2D Materials for Optoelectronics Science and Technology of Ministry of Education Institute of Microscale Optoelectronics, Shenzhen University, Shenzhen 518060, China. [4]Department of Chemistry, National University of Singapore, 3 Science Drive 3, Singapore 117543, Singapore. [5]Department of Physics and Shenzhen Key Laboratory of Advanced Quantum Functional Materials and Devices, Southern University of Science and Technology, Shenzhen, China. [6]These authors contributed equally: Chuanzhao Li, Mykola Telychko, Yue Zheng. ✉e-mail: hancheng@szu.edu.cn; kathy-kai.leng@polyu.edu.hk

presence of non-Ising or chiral components within DWs[8]. Ferroelectric DWs can adopt different internal structures, characterized as Néel or Bloch configurations. In a Néel-type wall, the polarization rotates in a plane perpendicular to the wall, while in a Bloch-type wall, it rotates within the plane parallel to the wall. These configurations can lead to distinct chiral characteristics based on how polarization changes direction across the wall. Additionally, ferroelectric domains can form ordered arrays that generate planar chirality arising from multi-polar effect[1]. Such planar chiral structure lacks a mirror plane and can rotate the polarization of transmitted light, leading to second harmonic generation with circular dichroism (SHG-CD).

Chiral DWs and domains are particularly relevant to improper ferroelectrics in hybrid organic-inorganic perovskites, where the ferroelectric polarization is induced by a secondary order parameter, like a structural distortion or octahedral tilt, rather than a primary order parameter such as the alignment of electric dipoles[2,9]. The discovery of domain-induced chirality in achiral ferroelectric crystals presents diverse potential applications. One significant advantage is the ability to simultaneously control electrical polarization and light propagation. This opens up possibilities for developing novel devices in quantum communication, where the manipulation of both electrical and optical signals is crucial. For example, the integration of chiral ferroelectric domains with waveguides or resonators could enable efficient control over the polarization state of light signals[10]. This could be utilized in the design of optical switches, modulators, or other components for quantum communication systems. However there has been a notable lack of research on the chiro-optical properties and atomic structure of ferroelectric domains and DWs in hybrid perovskite materials.

Herein, we investigate the planar chirality property and atomic structure of ordered ferroic domain arrays in two-dimensional (2D) Ruddlesden-Popper hybrid perovskites (RPPs) that possess either ferroelastic (lead iodide RPPs) or ferroelectric (lead bromide RPPs) properties. While both ferroelectric and ferroelastic 90°-twin domains exhibit linear dichroism, we observe planar chirality solely in the ferroelectric domains of 2D hybrid lead bromide perovskites for $n > 1$ homologues. Such planar chirality causes an automatic switching of

the SHG-CD response between adjacent 90°-twin ferroelectric domains with orthogonal polarizations. The QPlus-based atomic force microscopy (AFM) measurements reveal distinct arrangements of the atomic rows in ferroelastic and ferroelectric domains, giving rise to ferroelectric domain-specific chiral optical effect. Additionally, density functional theory (DFT) calculations further reveal ferroelectrically-switchable spin texture via ferroelectric polarization along either b or c- axis of the crystal between adjacent domains. The discovery of co-existing Rashba spin polarization, ferroelectricity and domain-induced chirality in these 2D hybrid perovskite domains paves the way for potential applications in domain-controlled optical memory, spin-logic devices and other chiral optoelectronic technologies.

Results and discussion

First, we examined the parallel striped domains in $n > 1$ homologues of $(BA)_2(MA)_{n-1}Pb_nBr_{3n+1}$ (Br-RPPs) and $(BA)_2(MA)_{n-1}Pb_nI_{3n+1}$ (I-RPPs) single crystalline films by polarized optical microscopy (POM) measurements (Fig. 1a and Supplementary Tables 1–3). These crystalline films were exfoliated from the as-prepared phase-pure centimeter-sized RPP bulk single crystals[11] (Supplementary Figs. 1–3). As shown in Fig. 1b, c, both types of ferroic films consist of quasi-one-dimensional (1D) stripes with widths ranging from 10 to 50 μm, and the bright-and-dark intensity modulation between adjacent domains arise from the spontaneous birefringence effect. Importantly, we observe that such longitudinal stripes are commonly found in $n > 1$ RPPs[12–14] and originate from the 90°-domain twinning. As depicted in Fig. 1a, rotation of the linear polarizer from 0° to 360° leads to a modulation of the light intensity with a period of 180° in each domain (Fig. 1d, e). The adjacent domains, labelled as A and B, host 90° phase difference between their periodic modulation originating from the orthogonal polar axes present in each domain (Supplementary Figs. 4–7). Two distinct configurations, referred to as type I and type II, can be identified with respect to the 90°-domain walls as depicted in Fig. 1f, appearing in different regions of the strip domains.

To verify the ferroelectric nature of the observed 1D domains in Br-RPPs with $n > 1$, we performed piezoresponse force microscopy (PFM) measurements. Figure 2a depicts the domain structure of $n = 2$
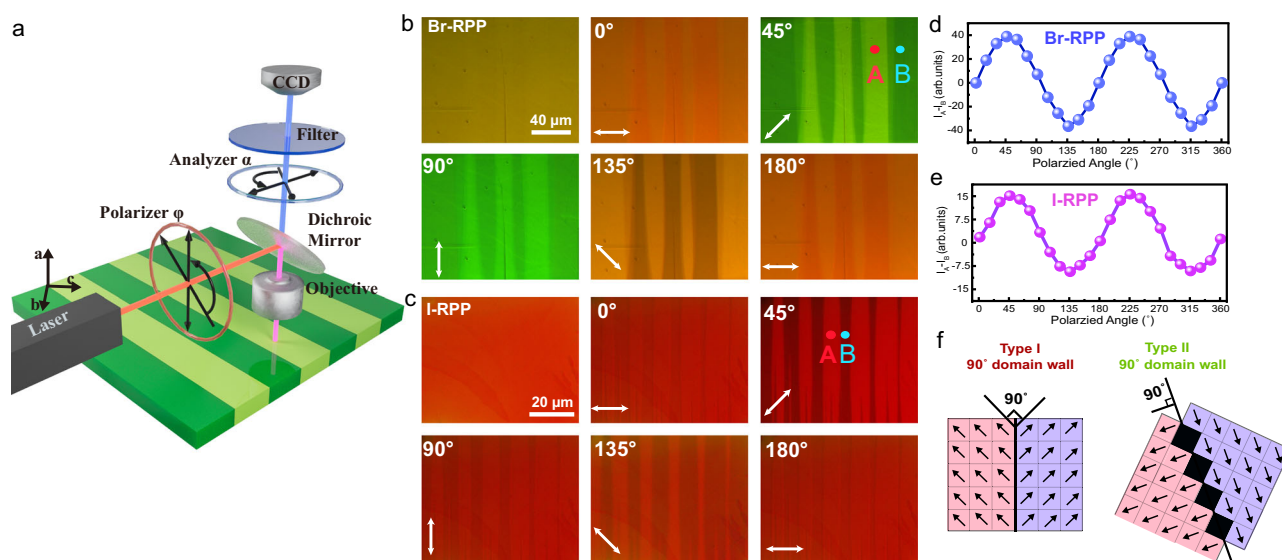

Fig. 1 | Optical detection of the 90°-domain twinning in crystalline striped ferroelectric and ferroelastic domains in the RPPs with $n > 1$. a Schematic illustration of angle-resolved polarized optical microscopy setup for measurement on domains. **b** A visual representation of color intensity contrast between adjacent ferroelectric domain A and B in $n = 2$ Br-RPP relative to the polarized light angle. **c** A visual representation of color intensity contrast between adjacent ferroelastic

domain A and B in $n = 2$ I-RPP relative to the polarized light angle. **d** The plot of contrast intensity change ($I_A - I_B$) between adjacent ferroelectric domains as a function of polarized angle from 0° to 360°. **e** The plot of contrast intensity change ($I_A - I_B$) between adjacent ferroelastic domains as a function of polarized angle from 0° to 360°. **f**, Two types of configurations for 90°-domain wall separation within striped ferroelectric or ferroelastic domains.
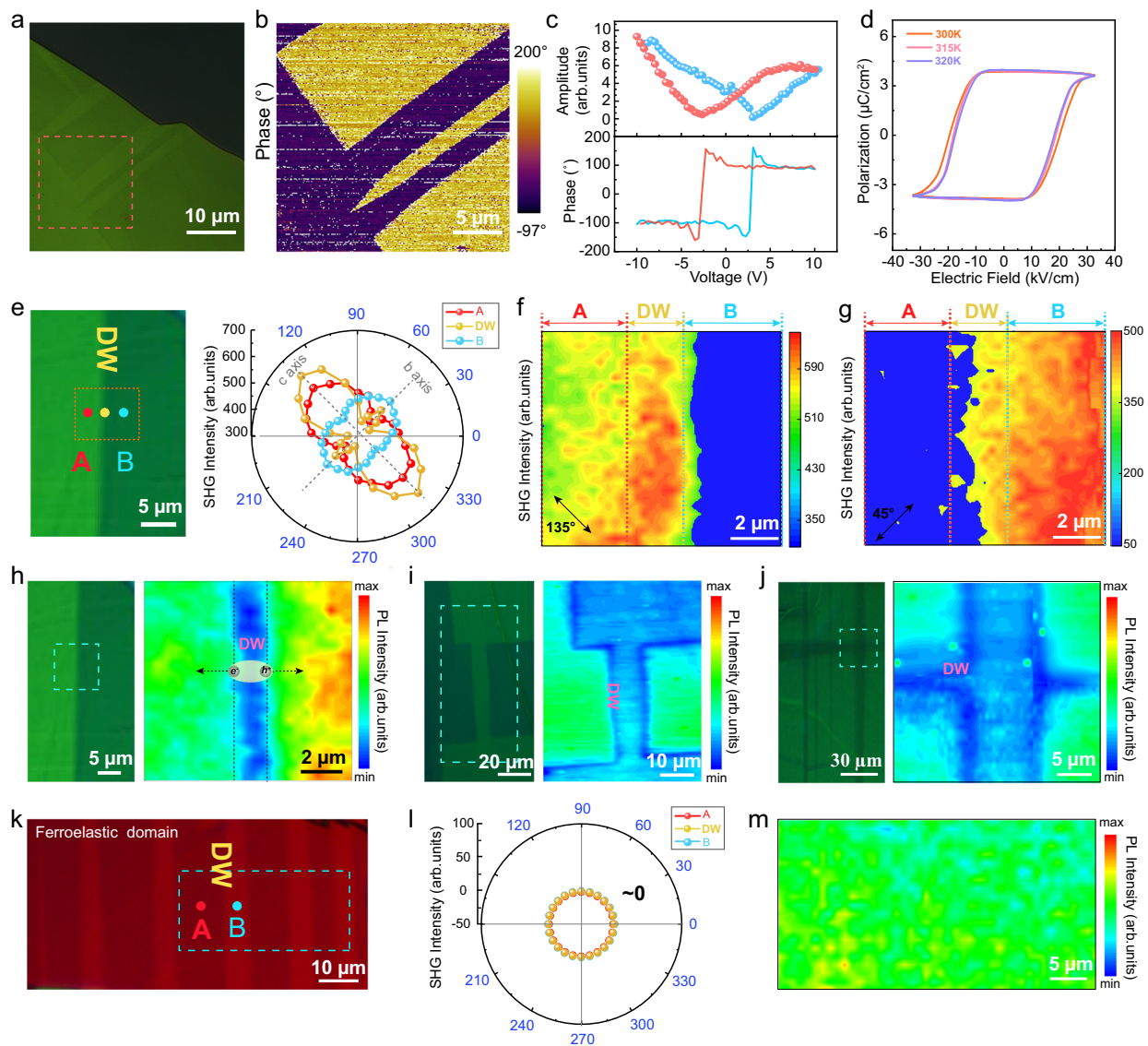
Fig. 2 | Distinctive optical properties in ferroelectric domains compared to ferroelastic domains in RPPs ($n > 1$). a The POM image of ferroelectric domains in $n = 2$ Br-RPP. **b** Corresponding lateral PFM phase image acquired in the region outlined by orange dashed rectangle in (**a**). The PFM lateral phase image unambiguously reveals the ferroelectric nature of the domains and DWs in $n = 2$ Br-RPP as evidenced by 180° phase contrast between adjacent bright- and dark domains. **c** Amplitude *vs* voltage and phase *vs* voltage curves in $n = 2$ Br-RPP. **d** Polarization vs electric field hysteresis loops taken at different temperatures in $n = 2$ Br-RPP. **e** Polarization-resolved SHG intensity measurements of ferroelectric domain A, B and domain wall (DW), separately. **f, g** Polarized SHG mapping of the area enclosed by a dashed rectangle in (**e**), at the polarized angle of 135° and 45°, respectively. **h–j** PL intensity mappings acquired over ferroelectric domains with distinct geometric shapes. The PL intensity signal is quenched at the DWs, as a result of the separation of photoexcited electron and hole pairs. **k** POM image of strip ferroelastic domains in $n = 2$ I-RPP. **l** Polar SHG plots of the area enclosed by a dashed rectangle in (**k**). **m** PL intensity mapping of the area enclosed by a dashed rectangle in (**k**).

Br-RPP revealed using POM, whilst Fig. 2b shows the corresponding piezoresponse phase map acquired in the region outlined by orange rectangle in Fig. 2a. The PFM lateral phase image unambiguously reveals the ferroelectric nature of the domains and DWs in $n = 2$ Br-RPP as evidenced by 180° phase contrast between adjacent bright- and dark domains. Figure 2c displays a butterfly-shaped amplitude hysteresis loop, indicative of the switchable ferroelectric polarization of domain. We also performed the PFM lithography to observe the ferroelectric domain reverse in $n = 2$ Br-RPP films, which further prove the ferroelectricity of $n > 1$ Br-RPPs (Supplementary Fig. 8). From the results of differential scanning calorimetry (DSC) in $n > 1$ Br-RPPs and I-RPPs, we found the ferroelectric Curie temperature (T_c) is ~352 K and ~315 K for $n = 2$ and $n = 3$ Br-RPP, respectively (Supplementary Fig. 9a, b and Supplementary Table 4). While the ferroelastic-paraelastic phase transition temperature for $n > 1$ I-RPPs is higher than 500 K (Supplementary Fig. 9c, d and Supplementary Table 4), which is well

consistent with the previous work[12]. Finally, we examined the ferroelectric characteristics of the crystals by acquisition of polarization *vs* electric field loops below T_c. The measurements revealed a polarization value of approximately 3.9 μC/cm² for $n = 2$ Br-RPP (Fig. 2d) and 2.6 μC/cm² for $n = 3$ Br-RPP (Supplementary Fig. 10). The polarization was found to be switchable when the applied positive or negative bias voltage exceeds the coercive voltage of the crystals. In contrast, such a polarization response was not observed on the ferroelastic crystals in I-RPPs with $n > 1$, consistent with its lack of ferroelectric polarisation.

Second harmonic generation (SHG) is a powerful technique for detecting polar phases as well as symmetry changes because SHG response is produced only in a non-centrosymmetric media and therefore, provides a background-free signal when the inversion symmetry is broken by the ferroelectric order[9,15–17]. As expected, no SHG response is detected on the crystals of ferroelastic I-RPPs with $n > 1$ and $n = 1$ Br-RPP due to its centrosymmetric structure. In contrast,

ferroelectric Br-RPPs with $n > 1$ reveal pronounced SHG response (Supplementary Fig. 11). To further demonstrate the presence of 90°-DWs within the ferroelectric domains, we conducted SHG polarimetry measurements. In Fig. 2e, we selected areas with well-defined ferroelectric domains for the polarization-resolved SHG analysis and mapping. In the case of a biaxial ferroelectric, linearly polarized SHG is expected to exhibit maximum signal along the polar b or c-axis. This is because the non-zero components of the second-order susceptibility tensor, d_{33}, d_{32} and d_{24} are largest along the polar b and c-axes of the crystal. For SHG measurements, we fixed the linear polarization of the detector to collect the 2ω signal along the b or c-axis of the crystal (Supplementary Fig. 12). Simultaneously, the polarization of the incident laser was rotated with frequency ω using a half-wave plate. The resulting polar plots of the domains A, B and DW displayed the SHG intensity as a function of the linear polarization orientation of the input laser. As shown in the polar SHG signal in Fig. 2e, the polarized axes of the largest linearly polarized SHG intensity at domains A and B are rotated by 90° with respect to each other in agreement with the aforementioned POM imaging results (Fig. 1d). We also performed polarized SHG mapping on the domains A, B, and DW within the region enclosed by a dashed rectangle in Fig. 2e. As depicted in Fig. 2f, g, there is a phase difference of 90° between the maximum SHG intensities of domain A and B, providing further evidence for the presence of a 90°-DW with the 90° phase modulation in ferroelectric domain of Br-RPPs with $n > 1$. Interestingly, the DW consistently displays stronger SHG signal than the domains, as shown in Fig. 2e, f. One explanation is that the polarization mismatch across the DW generates an electric field concentrated near the wall that enhances the SHG response[8]. We also performed linearly polarized SHG measurement on domain-free area (the region where the striped domains cannot be observed under POM) (Supplementary Fig. 13). The domain-free area shows a sharp figure-of-eight pattern consistent with the $mm2$ point group symmetry with two-fold rotation axes and two mirror planes. It can be seen that the polar maps of the domain A, B and DW regions are less symmetric with respect to the c-axis or b-axis compared to the domain-free region, indicating that the local mirror symmetry may be broken in the domains and DWs (Supplementary Fig. 13c).

Next, we investigate the impact of DWs on carrier recombination. Figure 2h shows a PL intensity mapping image acquired from two adjacent ferroelectric domains of $n = 2$ Br-RPP, separated by a DW, where the laser is focused on the dashed area in Fig. 2h (left). Notably, the PL signal was quenched at the DW, in contrast to the enhancement of the PL intensity signal in the domain area at either side of the DW. This behavior can be attributed to the existence of charged DW leading to the separation of photoexcited electron and hole pairs[5,18]. In addition, transfer of excitonic energy from the DW to the single domain area (domain A and domain B) also results in quenching of emission[19]. We extended our investigation to more complex geometric shapes of ferroelectric domains within the region framed by dashed rectangle in $n = 2$ Br-RPP (Fig. 2i, left and 2j, left). Among all tested samples, we consistently observed that the DWs exhibit a significantly lower PL intensity compared to the domain areas. This confirms that the ferroelectric DWs in 2D Br-RPPs effectively facilitate the separation of photoexcited electrons and holes. For comparison, we carried out analogous polarized SHG mapping and PL mapping on the ferroelastic domains of $n = 2$ I-RPP (Fig. 2k). In this case, neither the SHG response (Fig. 2l and Supplementary Fig. 14) nor the contrast in the PL intensity mapping (Fig. 2m) associated with ferroelastic DWs and domains was detected.

In a ferroelectric crystal, the arrangement of atoms within the crystal lattice is expected to render domains with opposing dipole orientations[2]. On the other hand, the formation of ferroelectric 90°-twin domains is triggered by strain compensation. Examining the atomic arrangement within ferroelectric and ferroelastic domains and uncovering their DW structures is useful for an in-depth understanding of how strain profile and charge order are expressed at nanoscale. However, achieving atomic imaging of 2D hybrid perovskites is challenging due to the insulating nature of the material[11,20]. To achieve non-invasive imaging of atomic structure of the ferroelectric and ferroelastic domains in hybrid perovskites, we utilized high-resolution non-contact atomic force microscopy (ncAFM) technique to study the domain atomic reconstruction of both Br-RPPs ($n = 1$–3) and I-RPPs ($n = 1$–3) crystals. Particularly, we applied QPlus-based imaging technique in frequency-modulation mode (See "Methods"). The ncAFM image directly interrogates the atomic arrangement of the apical inorganic Pb-X (X = Br, I) lattice[21] and the cooperative ordering of the underlying organic cations driven by their hydrogen bonding interactions with the inorganic lattice.

On both ferroelastic and ferroelectric domains of RPP with $n > 1$, the ncAFM images reveal dimer-like features arising from orthorhombic lattice relaxations. Taking $n > 1$ Br-RPP as an example, each dimer constitutes a pair of Br atoms located at the apices of two out-of-plane tilted $[PbBr_6]^{4+}$, similar to the octahedral tilt in I-RPP perovskites been reported by us previously[20]. However, a closer examination reveals markedly different atomic structure of the dimer rows in ferroelastic and ferroelectric RPPs. As shown in Fig. 3a, the ferroelastic $n = 3$ I-RPP crystal features large-area configurations of A' and B' where the orientation of the iodide dimer rows is unidirectional. In stark contrast, Fig. 3b shows that the ferroelectric $n = 3$ Br-RPP crystal is comprised of double-row dimers that are alternatingly oriented either along the [101] and [$\bar{1}$01] directions. As shown in Fig. 3c, each double-row dimer is color-coded by red and blue, representing an A-B-A-B configuration. We also observed the same A-B-A-B configuration in the ferroelectric $n = 2$ Br-RPP crystal (Fig. 3d). While twin-domains with uniformly two-unit cell widths (i.e. two rows of Br-dimers in each A or B) are hosted in the ferroelectric $n = 2$ Br-RPP, less regular twin-domain interspersed by rows of 2 to 3-unit cells, was observed in $n = 3$ Br-RPP (Fig. 3e). Because of this, the local glide mirror symmetry is broken.

We propose that the double-row-dimer structure observed in $n > 1$ Br-RPPs arises from a delicate balance of electrostatic forces resulting from the arrangement of methyl ammonium ions (MA$^+$)[22-24]. These ions are alternately positioned along A or B rows, as depicted by the yellow and pink arrows in Fig. 3f, respectively. Each A and B configuration is expected to exhibit a net nonzero polarization direction along the b and c-axes (purple arrow in Fig. 3g). Compared to non-ferroelectric $n = 1$ Br-RPP, the absence of the twin-domains (Br-dimers) and its nearly square 1×1 structure can be reconciled by absence of MA$^+$ chains to trigger out-of-plane octahedral tilting (Fig. 3h). We measured the lattice constants of a = 7.4 Å and b = 8.59 Å for $n = 2$ Br-RPP, whereas the ncAFM image of the $n = 1$ Br-RPP reveals nearly squared lattice with unit lattice constants a = 5.28 Å and b = 5.11 Å (Fig. 3i). QPlus AFM measurements conducted on adjacent polar A and B domains identified by POM earlier (Supplementary Fig. 15), reveal that they follow a type II configuration with 90°-domain wall separation, as shown in Fig. 1f. In contrast, the DW consists of a uniform square-like lattice structure with a finite width (Supplementary Fig. 15c), resembling that of the $n = 1$ Br-RPP.

We conducted DFT calculations to understand the electronic properties of ferroelectric domains. DFT calculations reveal that the in-plane ferroelectricity in $n > 1$ Br-RPPs leads to an out-of-plane Rashba effect observing unidirectional spin-splitting along the $\Gamma \to Y$ direction (Supplementary Fig. 16). The centrosymmetric paraelectric phase belongs to the space group of $I4/mmm$ with equivalent crystallographic c and b-axes[25]. Therefore, upon the system transitions to the ferroelectric phase, the crystal can be polarized either along the c (i.e., the c domain with space group $Cmc2_1$) or b (i.e., the b domain with space group $Bm2_1b$) direction[26], which correspond to $\pm k_y$ or $\pm k_x$ in the momentum space (Supplementary Fig. 16j). The intrinsic biaxial ferroelectric nature of the crystal, where polarization occurs along either
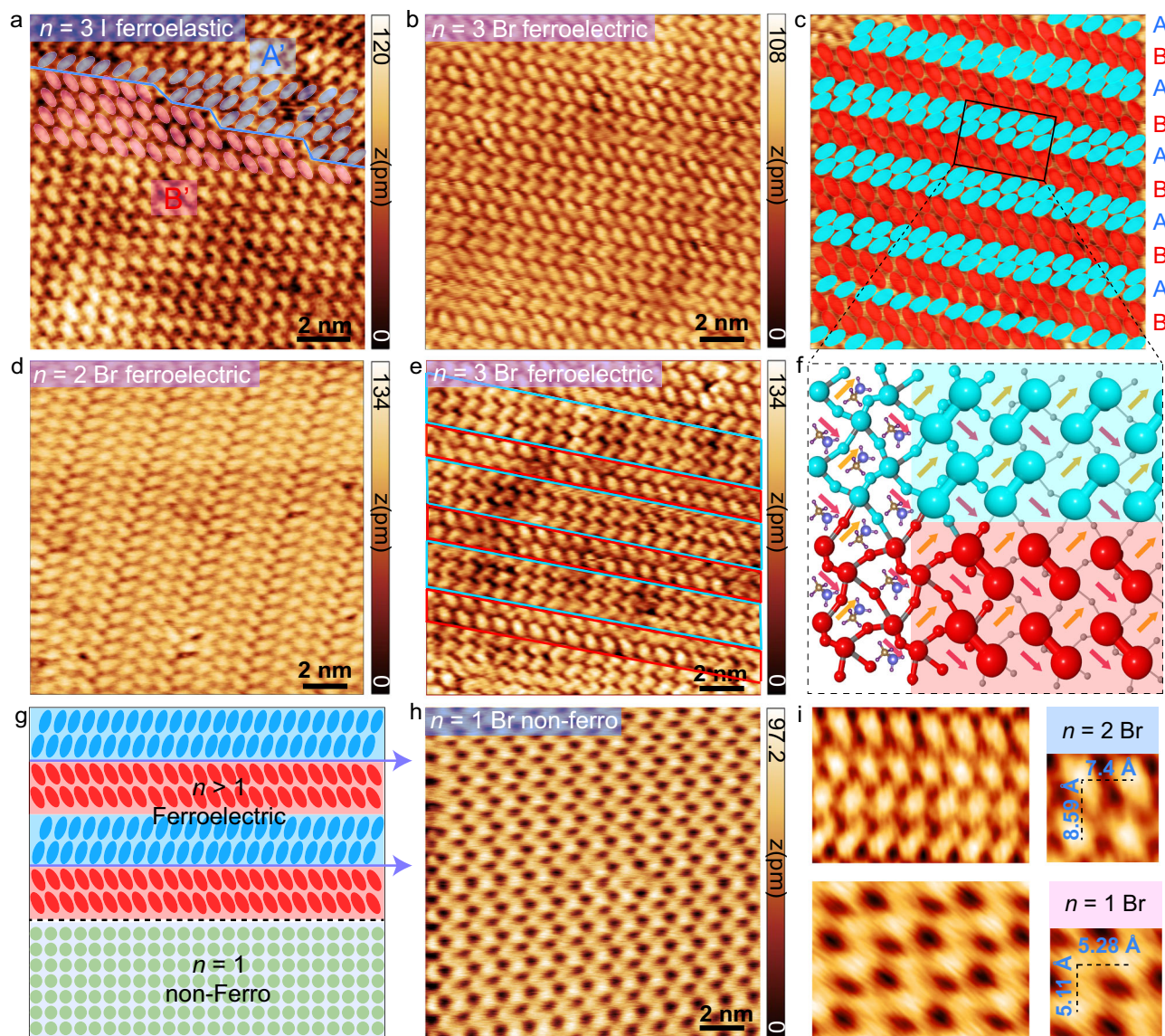
Fig. 3 | QPlus non-contact (nc) AFM imaging of surface symmetry in ferroelectric and ferroelastic RPP crystals. a ncAFM image of ferroelastic $n = 3$ I-RPP of large area I-dimer A′ and I-dimer B′ configurations occasionally separated by a twin-domain boundary indicated by a blue line. **b** ncAFM image of ferroelectric $n = 3$ Br-RPP of regular alternating arrangement of 2-unit cell width of twin-domain orientations. **c** Periodic A-B-A-B double-row arrangement in ferroelectric $n = 3$ Br-RPP surface. A and B double-row of Br-dimer orientations are indicated by blue and red, separately. **d** ncAFM image of ferroelectric $n = 2$ Br-RPP. **e** Less regular twin-domain arrangement with 2 to 3-unit cell width with local mirror symmetry breaking is also presented in ferroelectric $n = 3$ Br-RPP. **f** Schematic of the double-row Br-dimer twin structure alignment of inner MA$^+$ dipoles. Each blue or red dot represents a Br atom, while each arrow indicates the orientation of a dipole from the MA$^+$. **g** Vector addition of MA$^+$ dipoles resulting in a net polarization direction along the b and c-axes, indicated by the purple arrows in ferroelectric $n > 1$ Br-RPPs. This contrasts with the behavior observed in non-ferroelectric $n = 1$ Br-RPP. **h** Atomic image of non-ferroelectric $n = 1$ Br-RPP shows a nearly square structure. **i** A comparison of the atomic arrangement between ferroelectric $n = 2$ Br-RPP and non-ferroelectric $n = 1$ Br-RPP based on the lattice constants of each respective unit cell.

c or b-axis ($c \perp b$)[25], enables the spin texture to be switched between the 90°-twin domains[3], as shown in Supplementary Fig. 16k.

We utilized a two-photon photoluminescence excitation (TP-PLE) technique to investigate the Rashba splitting effect in both domain-free and domain-rich regions. The Rashba effect results in splitting of the bands in momentum space[17], leading to an increased number of accessible multiple pathways that contribute to the behavior of two-photon PL[27] (Supplementary Fig. 17 and Supplementary Note 1). Specifically, the split conduction band (CB) results in the formation of lower and upper branches. These branches serve as intermediate states for two-photon transitions to the upper and lower branches, respectively. As a result, the TP-PLE spectra exhibit an additional band slightly above the optical gap, which originate from the Rashba

splitting. The TP-PLE spectra reach maximum intensity when the energy of $2\hbar\omega$ exceeds the band-gap energy by $4E_R^{C(V)}$, where $E_R^{C(V)}$ represent the Rashba energy splitting associated with the conduction (valence) bands (Supplementary Fig. 18). Furthermore, the energy separation between the TP-PLE peak and the bandgap energy allows for the determination of the Rashba splitting energy.

The TP-PLE spectra acquired from the ferroelectric $n = 2$ Br-RPP domains are characteristic of inversion symmetry breaking and the presence of the Rashba splitting[17]. Firstly, we observed a shoulder feature near the onset of TP-PLE at approximately 2.80 eV. The shoulder demonstrates the two-photon allowed nature of the exciton transition via inversion symmetry breaking. Notably, this feature directly coincides with the peak position of the one-photon PL
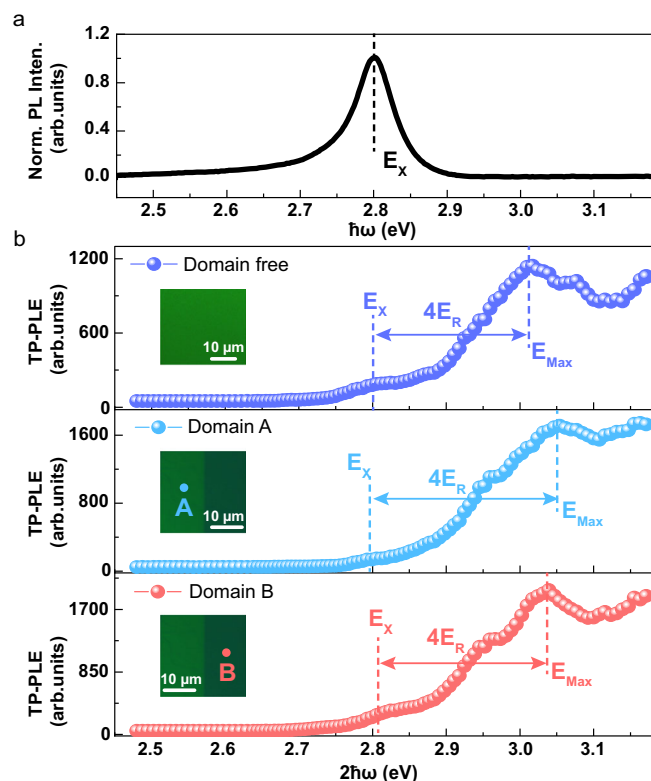
Fig. 4 | Rashba splitting revealed by two-photon photoluminescence excitation (TP-PLE) on exfoliated ferroelectric (BA)$_2$(MA)Pb$_2$Br$_7$ ($n = 2$) film with and without striped domains. a One-photon PL emission spectrum acquired on the surface of $n = 2$ Br-RPP film. **b** TP-PLE spectra of $n = 2$ Br-RPP film in three different regions: a domain-free area, domain A and domain B, as indicated by the respective inlet images. The positions of the exciton energy (E_X), Rashba splitting energy ($4E_R$) and energy of maximum PL intensity (E_{Max}) are designated on the spectra.

observed in these films (Fig. 4a). Secondly, we detected a prominent feature occurring above the bandgap, which is consistent with transitions between levels of the Rashba-split valence and conduction bands. The positions of these bands are identified to be approximately 0.217 eV, 0.261 eV, and 0.227 eV above the exciton energy for the areas of domain-free, domain A and B, respectively (Fig. 4b). Accordingly, we determined the Rashba energies (E_R) to be approximately 54 meV, 65 meV, and 57 meV for the domain-free area, domain A, and domain B, respectively (Supplementary Table 5). Our findings show that on average, the ferroelectric domains exhibit larger Rashba splitting energy as compared with the domain-free regions. The presence of chirality can introduce additional terms in the Hamiltonian that governs the Rashba effect. This can result in changes to the spin-orbit coupling strength and the spin-split energy levels.

Although the bulk film does not show any circular dichroism (CD) (Fig. 5a–c and Supplementary Fig. 19), we found that the ferroelectric domains can exhibit CD. To verify the emergence of chiro-optical effect, we used non-circularly polarized laser to focus on and excite the domains with the shortest lateral width >10 μm (Fig. 5d) and measured the difference between left-handed (L.H.) and right-handed (R.H.) emitted light by using a circularly polarised detector. The emitted PL from a region exhibiting CD is expected to show a strong bias for either left- or right-handed helicity. Accordingly, the measured polarization value P was calculated as (R.H. PL – L.H. PL)/(R.H. PL + L.H. PL). It is important to note that non-circularly polarized light does not selectively excite the Rashba-split states, thus the P value only reflects CD effect rather than Rashba spin-splitting effect. As depicted in Fig. 5e, we observed alternating sequence of positive and negative PL

polarization, indicated by a "red-yellow-red-yellow" pattern across the four A-B-A-B domains. This reflects a switching of chirality between adjacent domains. The absolute P values in these ferroelectric domains reached remarkable levels, with domain A exhibiting a value of $P_+ = 37.5\%$ and domain B exhibiting a value of $P = −20.3\%$ (Fig. 5f). These P magnitudes are among the highest values reported to date, even when compared to previously reported bulk chiral molecule-induced hybrid perovskites[28–30] (Supplementary Fig. 20 and Supplementary Table 6). In areas where we do not observe the striped domains under POM, the obtained P value is typically zero, suggesting that the CD arises solely from the ordered arrangement of domain or DW arrays. To rule out any potential interference from birefringence effects, we conducted a control experiment on the 90°-twin domains of ferroelastic $n = 2$ I-RPP (Fig. 5g). The result shows that P value was zero within the ferroelastic domains (Fig. 5h, i, Supplementary Fig. 21 and Supplementary Table 7), confirming that the observed phenomenon is not related to linear birefringence effects. It is worth noting that the high P value is obtained using ~445 nm emission, which corresponds to the deep-blue emission region. The observation of such a high chiro-optical effect in this spectral regime opens up new opportunities for chiral optoelectronic applications in the blue and violet wavelength range (Supplementary Fig. 22).

In addition, the existence of domain-switchable chirality is further confirmed through the observation of circularly polarized second harmonic generation (SHG) from the domains and DWs when these were excited with linearly polarized laser. Because the SHG signals from DWs were observed to be overwhelmingly stronger compared with the domains, we focus our discussion on the SHG-CD effect coming from the DWs in Fig. 5j–l and Supplementary Fig. 23. Interestingly, the handedness of the circularly polarized SHG signal is switched between the adjacent DWs, which accords with the switching of the ferroelectric polarization of the domains by 90° at both sides of the DW (Fig. 5m). Figure 5l shows alternating σ + and σ- SHG signals for DW1, DW2 and DW3. Remarkably, the anisotropy factor ($g_{SHG−CD}$) used to quantify the SHG-CD effect is an impressive 0.41 for the DW, compared to 0.18 on the ferroelectric domains (see detailed calculation in Methods). This DW-specific SHG-CD effect is among the highest chiral optical response reported, even when compared to chiral molecule induced hybrid perovskites (Supplementary Table 8)[31–33].

The nonlinear optical susceptibility tensor governing the SHG process is influenced by the system's symmetry and ferroic order[34]. Both (BA)$_2$(MA)Pb$_2$Br$_7$ and (BA)$_2$(MA)$_2$Pb$_3$Br$_{10}$ crystals exhibit C_{2v} ($mm2$) point group symmetry below the T_c, characterized by a twofold rotation axis along the z- direction and two mirror planes parallel to the y-z and x-z planes. In the orthogonally polarized ferroelectric domains, the symmetry is reduced from $mm2$ to lower point group 1 or m with one mirror plane parallel to the y-z plane and no glide mirror planes perpendicular to the y-z plane. Thus, planar chirality can emerge (see Supplementary Note 2). The second-order susceptibility tensor responsible for SHG is a second-rank tensor, which means it has components that depend on multiple directions. In orthogonally aligned domains, the susceptibility tensor accounts for the anisotropic response of the material to an applied electric field or circularly polarized light. A distinctive feature of ferroelectric Br-RPP is the ordered striped array of ferroelectric domains, where the polarization of the domains switches by 90° across the DWs, as illustrated in Fig. 5m. In this ordered array, the DW traverses two ferroelectric domains with orthogonal electric polarizations. This multi-polar domain effect explains why we observed a stronger SHG-CD at DW compared to single-domain regions (Supplementary Figs. 23, 24). When circularly polarized light interacts with the orthogonal domains, the electric field components of the light induce polarization changes in both domains. Due to the 90° angle between their polarizations, the response from one domain becomes out of phase with the response from the other domain, resulting in a π/2 phase shift between the
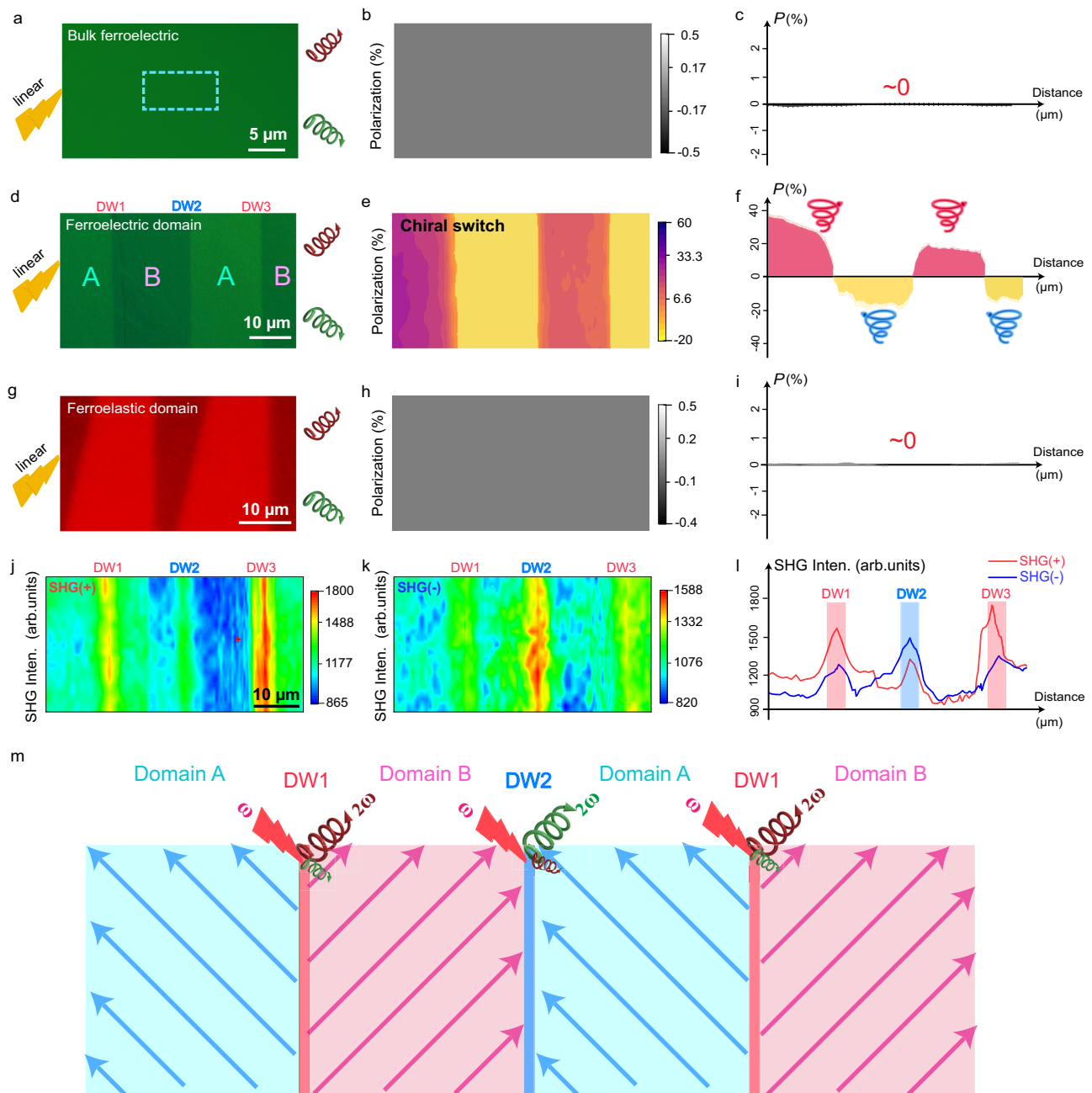
Fig. 5 | Domain-induced switching of spin polarization and SHG circular dichroism in ferroelectric hybrid perovskite domains. a Optical image of $n = 2$ Br-RPP without domains upon excitation with linearly polarized light. **b** Polarization (P) mapping. **c** Corresponding oscillation of P, showing a zero value. **d** Optical image of $n = 2$ Br-RPP with A-B-A-B ferroelectric domains under linearly polarized light excitation. **e** P mapping under linearly polarized light excitation, indicating a chirality switch. **f** Corresponding oscillation of P values across A-B-A-B domains. **g** Optical image of ferroelastic $n = 2$ I-RPP under linearly polarized light excitation. **h** Resulting P mapping showing negligible response. **i** Corresponding oscillation of P values, showing a zero value. **j** SHG-CD mapping on sample in (**d**) under linearly polarized light excitation and right-handed polarized light ($\sigma +$) detection. **k** Circular dichroism SHG mapping on sample in (**d**) under linearly polarized light excitation and left-handed polarized light (σ-) detection. **l** Comparison of SHG intensity difference at domain walls (DWs) in (**j**, **k**). **m** Schematic illustrating the orthogonally polarized ferroelectric domains separated by DWs, where a strong SHG-CD response is observed at the DWs with reversed ferroelectric polarization.

polarizations induced in the two domains. This phase difference leads to a sign reversal of the second-order susceptibility tensors in adjacent domains (see Supplementary Note 3).

In summary, we have observed strong domain-specific circular dichroism, and Rashba spin-splitting in highly ordered 90°-twin domains of ferroelectric hybrid perovskites. Although the bulk Br-RPP crystals with $n > 1$ are achiral, each ferroelectric domain exists as chiral enantiomers, coupled in the opposite sense to their parallel-aligned neighbors, leading to planar chirality. The $\pi/2$ phase shift that occurs in

orthogonally polarized ferroelectric domains results in a switching of the circular dichroic response in adjacent domains and DWs. This phenomenon arises from the interplay between the polarization states, the nonlinear optical susceptibility tensor, and the phase relationships between the induced polarizations. An intriguing consequence of this phenomenon is the simultaneous switching of both Rashba spin texture and chirality with the alternation of b and c-axis ferroelectric polarization in adjacent parallel-aligned domains. The interplay between chirality and spin texture in these ferroelectric domains can

potentially enable the development of innovative optical logic devices. For example, chiral DWs can act as stable domain boundaries, enabling the creation of non-volatile memories with distinct spin configurations. By leveraging the unique properties of chiral domains and DWs, such as their distinct spin configurations and transport characteristics, it may be possible to design logic gates and circuits that utilize chirality as an additional degree of freedom.

In terms of chiro-optical applications, we observe that ferroelectric domains and DWs in the achiral Br-RPP crystals ($n > 1$) exhibit large SHG-CD ratios comparable to the highest values reported in macroscopic chiral molecule-induced bulk hybrid perovskite crystals. This result has important implications for understanding how the spatial distribution of electric field and strain gradients can be harnessed to design metasurfaces with strong SHG-CD, even in globally achiral crystal. Chiral ferroelectric domains can be incorporated into metamaterials and have significant potential for applications in electrically switchable nonlinear optics, such as chiral sensing, chiral imaging, and chiral light manipulation. Future research may investigate how to control the spatial orientation and size of the ferroelectric domains through electric field poling, temperature gradient poling, or mechanical stress-induced alignment to enhance the nonlinear optical response.

Methods

Synthesis of Br-RPPs and I-RPPs single crystals
We procured lead oxide (PbO) powders, hydroiodic acid (HI, 57 wt % in H_2O), hydrobromic acid (HBr, 48 wt% in H_2O), and hypophosphorous acid (H_3PO_2, 50 wt% in H_2O) from Sigma-Aldrich. Additionally, we sourced methylammonium bromide (MABr), methylammonium iodide (MAI), n-butylammonium bromide (BABr), and n-butylammonium iodide (BAI) from Greatcell Solar Ltd. All these chemicals were used as received for the experiment.

To synthesize phase-pure $(BA)_2(MA)_{n-1}Pb_nBr_{3n+1}$ ($n = 1-3$) single crystals, it is crucial to determine the correct molar ratios of precursors. To ensure the growth of large-sized single crystals, an appropriate cooling rate must be maintained.

The molar ratio of BABr, MABr, and PbO identified for synthesizing phase-pure $(BA)_2(MA)_{n-1}Pb_nBr_{3n+1}$ are as follows: 0.59 M, 0 M, and 0.40 M for $(BA)_2PbBr_4$ ($n = 1$); 0.59 M, 0.21 M, and 0.40 M for $(BA)_2(MA)Pb_2Br_7$ ($n = 2$); and 0.59 M, 0.21 M, and 0.40 M for $(BA)_2(MA)_2Pb_3Br_{10}$ ($n = 3$). Each batch of powders was placed in a mixed solution of HBr and H_3PO_2 (9:1, vol/vol) and then heated to 120 °C while stirring for 40 mins, resulting in a clear and transparent solution. To cool the mixture to room temperature, we applied a rate of 1 °C per day, allowing large single crystals of $n = 1, 2$ and 3 bromides to form. Finally, we dried the crystals in a vacuum chamber overnight.

The method for synthesizing phase-pure, large-sized $(BA)_2(MA)_{n-1}Pb_nI_{3n+1}$ ($n = 1-3$) single crystals has been described in our previous work[11].

PXRD and single-crystal structure determination
PXRD was performed on Rigaku SmartLab X-ray diffractometer using *Cu Kα* radiation. Single crystal X-ray diffraction (SC-XRD) intensity data for ferroelectric RPPs were collected at both low and high temperatures, respectively. The measurements were conducted using a four-circle goniometer with Kappa geometry and a Bruker AXS D8 Venture Single Crystal X-ray Diffractometer equipped with a Photon 100 CMOS active pixel sensor detector. Data collection, data reduction, and absorption correction were carried out using the software package of APEX3 (Supplementary Tables 1–3). All calculations for structure determination were carried out using the SHELXTL package. 3. Data are available from the corresponding author on request.

Angle-resolved polarized optical microscopy
The Leica CCD captured optical images of ferroelectric and ferroelastic striped domain patterns at room temperature. A polarizer was positioned in front of the CCD for angle-resolved polarized optical capture (Fig. 1a). While maintaining a fixed orientation of the ferroelectric and ferroelastic polarization axis in domain A and B, we varied the angle of the polarized light from 0° to 360°. In principle, when the polarized axes of the ferroelectric domains are parallel to the direction of the polarized light, the collected optical microscopy image appears brightest. Conversely, if the axes are not parallel, the color appears relatively darker. To quantify the color contrast intensity change between domain A and B (I_A-I_B) as a function of the polarized light angle, we utilized the commercial ImageJ software. The results are illustrated in Fig. 1d, e.

PFM and ferroelectricity measurement
PFM measurements were conducted using a commercial atomic force microscope (Asylum Research MFP-3D) at room temperature. Pt/Ir-coated conductive tips (2.8 N/m) was used and an AC drive voltage of 1–2 V was employed under a contact resonant frequency of ~340 Hz during all the PFM measurements. To measure the ferroelectricity of crystals, the bulk single crystals of $(BA)_2(MA)Pb_2Br_7$ ($n = 2$) and $(BA)_2(MA)_2Pb_3Br_{10}$ ($n = 3$) that covered with silver conducting paste on the surfaces. The ferroelectric hysteresis loops presented in Fig. 2d were obtained using a double-wave method on a Radiant Precision Premier II instrument. During ferroelectric experiments, well-developed single crystals of $n > 1$ Br-RPP were cut with the orientation along the crystallographic *c*-axis and coated with silver conducting paste on the *ab* plane. To prevent electric discharge at high electric field or high temperature, the samples were immersed in silicone oil during the measurement. The temperature was carefully controlled using an oil bath.

Differential scanning calorimetry (DSC) measurement
DSC analyses of Br-RPPs and I-RPPs single crystals were performed using a Mettler Toledo DSC3 instrument. The measured temperature ranges for $n = 2$ Br-RPP, $n = 3$ Br-RPP, $n = 2$ I- RPP, and $n = 3$ I-RPP are 300–380 K, 295–335 K, 300–500 K, and 300–500 K, respectively. The crystalline samples were placed in aluminum crucibles that were heated and cooled with a rate of 10 K/min under the nitrogen atmosphere.

Polarization-resolved SHG microscopy
SHG spectra and spatial mapping were performed in high-vacuum conditions at 77 K using a confocal Metatest ScanPro Laser Scanning System (ScanPro Advance, Metatest). An excitation laser with the wavelength of 1064 nm (Rainbow 1064 OEM) was employed, and the linearly polarized laser beam was focused using a ×50 objective lens with a NA of 0.7. For the linearly polarized SHG measurement, a half-wave plate was utilized to control the polarization of the laser (Supplementary Fig. 12). To acquire SHG spectra at different polarization angles as shown in Fig. 2e–g, the polarization of the incident laser was rotated using a manual half-wave plate.

Non-polarized PL measurement
For the non-polarized PL experiments shown in Fig. 2h–j, m, a 405 nm continuous wave (CW) laser (ALPHALAS) was used to excite the surface of the ferroelectric and ferroelastic striped domains of $n = 2$ RPP under high-vacuum conditions at 77 K. In this setup, there were no polarizer or quarter-waveplate ($\lambda/4$) plate in the optical path.

QPlus ncAFM measurement
QPlus ncAFM measurements were conducted under ultrahigh-vacuum conditions at 77 K using a commercial Omicron LT STM/AFM system. To acquire topography AFM images, a constant-frequency-shift mode was employed. The measurements were carried out using QPlus sensors with a resonant frequency of 28.2 kHz and a quality factor of 10,000.

Two-Photon photoluminescence excitation (TP-PLE) measurement

The excitation light source was a tunable ultrafast laser (Spectra-Physics Insight X3) with variable output. The laser was focused by a ×25 microscope objective lens, which generates pulses of ~170 fs duration in the spectral range of 0.95–1.80 eV. The spot size of the laser was ~1 μm, and the spectra were recorded using a Nikon spectrometer at room temperature. The integrated light intensity in the 442–444 nm region were monitored. To obtain the normalized result, we divided the integrated PL intensity by the square of the laser power at each excitation wavelength.

Circularly polarized PL measurement

Circularly polarized PL measurement is performed using linearly polarized light for excitation and circular polarization for detection. In detail, a 405 nm continuous wave (CW) laser (ALPHALAS) was used to excite the surface of the single crystalline ferroelectric or ferroelastic strip domains of RPP with $n = 2$, as shown in Fig. 5a, d, g. The optical setup is depicted in Supplementary Fig. 19a, the linear polarizer (P1) was fixed in the incident beam path to clean the initial polarization of the laser, which was set to s-polarization. To control the excited laser as linear polarization, no quarter-waveplate ($\lambda/4$) plate was used in the incident light path. However, the back-scattered PL was collected and passed through a $\lambda/4$ plate. Another linear polarizer P2 was also fixed in the s-polarized orientation and placed in the detection beam path (Supplementary Fig. 19a). Setting the s-polarization as the 0° reference, we could achieve σ + /σ- polarized detection by adjusting the $\lambda/4$ plate's fast axis to +45°/−45° relative to the s-polarization direction. The PL signals were detected by a spectrometer (Acton, Spectra Pro HRS-500) and a charged-coupled device (Princeton Instruments, Pixis 400B). A cryostat was used to study the circularly polarized PL at 77 K. Thus, we were able to measure the PL intensities and mappings under linearly polarized excitation and circular polarized detection (linear/σ+ and linear/σ-), respectively.

SHG-CD measurement

A 1064 nm continuous wave (CW) laser (Rainbow 1064 OEM) was used to excite the surface of the ferroelectric strip domains of RPP with $n = 2$ as shown in Fig. 5j–l. The optical setup is depicted in Supplementary Fig. 23a. A linear polarizer (P1) was fixed in the incident beam path to clean the initial polarization of the laser, which was set to s-polarization. To control the excited light as linear polarization, no quarter-waveplate ($\lambda/4$) plate was used in the incident light path. However, the back-scattered PL was collected and passed through a $\lambda/4$ plate. Another linear polarizer P2 was also fixed in the s-polarized orientation and placed in the detection beam path (Supplementary Fig. 23a). Setting the s-polarization as the 0° reference, we could achieve σ + /σ- polarized detection by adjusting the $\lambda/4$ plate's fast axis to +45°/−45° relative to the s-polarization direction. The SHG signals were detected by a spectrometer (Acton, Spectra Pro HRS-500) and a charged-coupled device (Princeton Instruments, Pixis 400B). A cryostat was used to study the SHG-CD mappings and spectra at 77 K. Thus, the intensities of SHG under (linear/σ+ and linear/σ-) excitation/detection can be detected, respectively.

g_{SHG-CD} factor calculation

The SHG-CD effect is quantified by the corresponding anisotropy factor (g_{SHG-CD}), which is defined as: $g_{SHG-CD} = |2(I_{LCP}-I_{RCP})|/(I_{LCP} + I_{RCP})$, where I_{LCP} and I_{RCP} represent the SHG intensity upon detection with left-handed and right-handed circular polarization, respectively. For the domain wall, the measured values are $I_{LCP} \approx 1180$ and $I_{RCP} \approx 1798$ (Supplementary Fig. 23e). For the domain, the measured values are $I_{LCP} \approx 1002$ and $I_{RCP} \approx 1202$ (Supplementary Fig. 23f). Using these values, the calculated g_{SHG-CD} for the domain wall is 0.41, while the value for the domain is 0.18.

Computational method

All the simulations were performed using the density functional theory (DFT) software package VASP. We employed a plane-wave basis set together with the projected augmented wave potentials from the VASP standard library. The generalized gradient approximation in the form of the Perdew-Burke-Ernzerhof functional was adopted to describe the exchange-correlation energy, and the DFT-D3 method was used to account for van der Waals interaction within the system. The energy cutoff was set to 600 eV and a $1 \times 5 \times 5$ k-point grid was used for the $(BA)_2(MA)Pb_2Br_7$ unit cell. All the structures were fully optimized until the forces between atoms were smaller than 0.002 eV·Å^{-1}. As the system contains the heavy element Pb and is found to exhibit spin splitting experimentally, we also included spin-orbit coupling (SOC) in the investigation of the electronic properties.

Data availability

All data generated and analyzed in this study are included in the Article and its Supplementary Information, and are also available from authors upon request.

References

1. Papakostas, A. et al. Optical manifestations of planar chirality. *Phys. Rev. Lett.* **90**, 107404 (2003).
2. Gou, J. et al. Two-dimensional ferroelectricity in a single-element bismuth monolayer. *Nature* **617**, 67–72 (2023).
3. Guo, W. et al. Electrically switchable persistent spin texture in a two-dimensional hybrid perovskite ferroelectric. *Angew. Chem. Int. Ed.* **135**, e202300028 (2023).
4. Kumari, P., Basnet, B., Lavrentovich, M. O. & Lavrentovich, O. D. Chiral ground states of ferroelectric liquid crystals. *Science* **383**, 1364–1368 (2024).
5. Qian, Q. et al. Photocarrier-induced persistent structural polarization in soft-lattice lead halide perovskites. *Nat. Nanotechnol.* **18**, 357–364 (2023).
6. Vizner Stern, M. et al. Interfacial ferroelectricity by van der Waals sliding. *Science* **372**, 1462–1466 (2021).
7. Ramesh, R. et al. Dynamics of ferroelastic domains in ferroelectric thin films. *Nat. Mater.* **2**, 43–47 (2003).
8. Cherifi-Hertel, S. et al. Non-Ising and chiral ferroelectric domain walls revealed by nonlinear optical microscopy. *Nat. Commun.* **8**, 15768 (2017).
9. Leng, K., Li, R. L., Lau, S. P. & Loh, K. P. Ferroelectricity and Rashba effect in 2D organic-inorganic hybrid perovskites. *Trends Chem.* **3**, 716–732 (2021).
10. Shafer, P. et al. Emergent chirality in the electric polarization texture of titanate superlattices. *Proc. Natl. Acad. Sci.* **115**, 915–920 (2018).
11. Leng, K. et al. Molecularly thin two-dimensional hybrid perovskites with tunable optoelectronic properties due to reversible surface relaxation. *Nat. Mater.* **17**, 908–914 (2018).
12. Xiao, X. et al. Layer number dependent ferroelasticity in 2D Ruddlesden-Popper organic-inorganic hybrid perovskites. *Nat. Commun.* **12**, 1332 (2021).
13. Liu, Y. et al. Chemical nature of ferroelastic twin domains in $CH_3NH_3PbI_3$ perovskite. *Nat. Mater.* **17**, 1013–1019 (2018).
14. Wang, J. et al. Unusual ferroelectric-dependent birefringence in 2D trilayered perovskite-type ferroelectric exploited by dimensional tailoring. *Matter* **5**, 194–205 (2022).
15. Du, Y. et al. A homochiral fulgide organic ferroelectric crystal with photoinduced molecular orbital breaking. *Angew. Chem. Int. Ed.* **62**, e202315189 (2023).
16. Abdelwahab, I. et al. Giant second-harmonic generation in ferroelectric $NbOI_2$. *Nat. Photonics* **16**, 644–650 (2022).
17. Stranks, S. D. & Plochocka, P. The influence of the Rashba effect. *Nat. Mater.* **17**, 381–382 (2018).

18. Huxter, W. S., Sarott, M. F., Trassin, M. & Degen, C. L. Imaging ferroelectric domains with a single-spin scanning quantum sensor. *Nat. Phys.* **19**, 644–648 (2023).

19. Li, C., Loh, K. P. & Leng, K. Organic-inorganic hybrid perovskites and their heterostructures. *Matter* **5**, 4153–4169 (2022).

20. Shao, Y. et al. Unlocking surface octahedral tilt in two-dimensional Ruddlesden-Popper perovskites. *Nat. Commun.* **13**, 138 (2022).

21. Telychko, M. et al. Sub-angstrom noninvasive imaging of atomic arrangement in 2D hybrid perovskites. *Sci. Adv.* **8**, 0395 (2022).

22. She, L., Liu, M. & Zhong, D. Atomic structures of $CH_3NH_3PbI_3$ (001) surfaces. *ACS Nano* **10**, 1126–1131 (2016).

23. Stecker, C. et al. Surface defect dynamics in organic–inorganic hybrid perovskites: from mechanism to interfacial properties. *ACS Nano* **13**, 12127–12136 (2019).

24. Ohmann, R. et al. Real-space imaging of the atomic structure of organic–inorganic perovskite. *J. Am. Chem. Soc.* **137**, 16049–16054 (2015).

25. Qin, Y. et al. Dangling octahedra enable edge states in 2D lead halide perovskites. *Adv. Mater.* **34**, 2201666 (2022).

26. Li, L. et al. Two-dimensional hybrid perovskite-type ferroelectric for highly polarization-sensitive shortwave photodetection. *J. Am. Chem. Soc.* **141**, 2623–2629 (2019).

27. Lafalce, E. et al. Rashba splitting in organic-inorganic lead-halide perovskites revealed through two-photon absorption spectroscopy. *Nat. Commun.* **13**, 483–483 (2022).

28. Qin, Y. et al. Multifunctional chiral 2D lead halide perovskites with circularly polarized photoluminescence and piezoelectric energy harvesting properties. *ACS Nano* **16**, 3221–3230 (2022).

29. Wang, J. et al. Aqueous synthesis of low-dimensional lead halide perovskites for room-temperature circularly polarized light emission and detection. *ACS Nano* **13**, 9473–9481 (2019).

30. Liu, S. et al. Bright circularly polarized photoluminescence in chiral layered hybrid lead-halide perovskites. *Sci. Adv.* **9**, 5083 (2023).

31. Fu, D. et al. Chirality-dependent second-order nonlinear optical effect in 1D organic–inorganic hybrid perovskite bulk single crystal. *Angew. Chem. Int. Ed.* **133**, 20174–20179 (2021).

32. Fu, X. et al. Highly anisotropic second-order nonlinear optical effects in the chiral lead-free perovskite spiral microplates. *Nano Lett.* **23**, 606–613 (2023).

33. Wang, H. et al. Chiral hybrid germanium (II) halide with strong nonlinear chiroptical properties. *Angew. Chem. Int. Ed.* **135**, e202309600 (2023).

34. Denev, S. A., Lummen, T. T. A., Barnes, E., Kumar, A. & Gopalan, V. Probing ferroelectrics using optical second harmonic generation. *J. Am. Ceram. Soc.* **94**, 2699–2727 (2011).

Acknowledgements

Author contributions

K.L. and C.L. conceived and designed the experiments. K.L. supervised the research. C.L. fabricated all perovskite single crystals. C.L. prepared all exfoliated films and performed POM measurements. M.T. performed the QPlus ncAFM measurement. J.L. contributed to the analysis of the atomic structure. C.L. and Y.Z. performed all the optical measurements. C.H. supervised the testing of optical measurements. S.Y. performed DFT calculations. C.L. and Z.W. measured the P-E loops. W.P.D.W. and Z.W. performed single-crystal XRD structural analysis. Y.L., W.F.I., X.W. and J.H. performed the PFM measurements. Y.J. performed the XRD measurements. K.L. and C.L. wrote the manuscript.

Competing interests

The authors declare no competing interests.

Additional information

Supplementary information The online version contains supplementary material available at https://doi.org/10.1038/s41467-024-54524-3.

Correspondence and requests for materials should be addressed to Cheng Han or Kai Leng.

Peer review information *Nature Communications* thanks the anonymous reviewer(s) for their contribution to the peer review of this work. A peer review file is available.

Reprints and permissions information is available at http://www.nature.com/reprints

Publisher's note Springer Nature remains neutral with regard to jurisdictional claims in published maps and institutional affiliations.